Plasmonic AuPd-based Mott-Schottky photocatalyst for synergistically enhanced hydrogen evolution from formic acid and aldehyde

Shengbo Zhang[a,1], Mei Li[a,1], Jiankang Zhao[a,1], Hua Wang[a], Xinli Zhu[a], Jinyu Han[a], Xiao Liu[b,a,*]

[a] Key Laboratory for Green Chemical Technology of the Ministry of Education, School of Chemical Engineering and Technology, Collaborative Innovation Center of Chemical Science and Engineering, Tianjin University, Tianjin, 300072, PR China
[b] Key Laboratory of Pesticide & Chemical Biology of the Ministry of Education, College of Chemistry, Central China Normal University, Wuhan, 430079, PR China

A B S T R A C T

Plasmonic AuPd alloy nanoparticles supported on super small carbon nitride nanospheres (Au_xPd_y/CNS) for the design of Mott-Schottky catalysts were successfully synthesized and further applied for the photocatalytic hydrogen evolution from formic acid. A high turnover frequency (TOF) value of 1017.8 h^{-1} was obtained for the AuPd/CNS catalyst under visible-light irradiation (λ > 420 nm) at 298 K. XPS analysis, photoelectrochemical characterization and density functional theory (DFT) calculation indicate that the remarkable photocatalytic activities are mainly attributed to the optimized electronic structure of Pd in the AuPd/CNS composite resulting from the alloying, plasmonic and Mott-Schottky effects. These effects can efficiently accelerate the electron transfer from photoresponsive super small carbon nitride nanospheres and plasmonic Au to the active Pd sites. We also infer that the alloying effect is the main factor on the high activity, which is mainly due to weakened adsorption of hydrogen atoms on Pd sites according to the DFT calculation. Moreover, the Mott-Schottky AuPd/CNS catalyst presents a good universality for the photocatalytic hydrogen evolution from a series of aldehyde aqueous solutions.

1. Introduction

Hydrogen fuel, one of the cleanest energy sources, has drawn wide attention in electrochemical cells or internal combustion engines to power vehicles or electric devices [1–5]. However, the controllable storage and safe delivery of hydrogen still limit its wide application. Recently, liquid-phase chemical hydrogen storage materials, such as formic acid, methanol, ammonia borane and formaldehyde have been intensively studied [6–14]. Among them, formic acid is a promising hydrogen carrier because of its high hydrogen capacity (4.4 wt %), non-toxicity, good stability and easy accessibility. Many studies have confirmed that Pd-based catalysts are the most effective catalysts for hydrogen evolution from formic acid, especially bimetallic AuPd, AgPd, NiPd, etc. However, this reaction is usually carried out at high temperature because the dehydrogenation pathway is thermodynamically favored ($\Delta G = -48.8$ kJ mol) [15–26]. It is still required to develop efficient and energy-saving methods for hydrogen evolution from liquid-phase hydrogen storage materials.

Light-driven decomposition of hydrogen-containing compounds under the room temperature is a promising approach for hydrogen evolution. Recently, we reported the visible-light-driven hydrogen evolution from formaldehyde-water solution using AuPd nanoparticles supported on novel solid mesoporous organosilica nanotubes [13]. However, inert organosilica nanotubes supports are insensitive to light, which severely affects the separation efficiency of the photogenerated charges. To accelerate charge kinetics of the photocatalytic reaction, integrating the metals (such as Pd, Au, Ag and Pt) and the semiconductors to construct Mott-Schottky photocatalysts is an effective method for improving the photocatalytic performance [27–30]. Graphitized carbon nitride (g-C_3N_4) with a band gap of 2.7 eV can be used not only as a photoresponsive catalyst [31–36], but also as an excellent carrier to stabilize metal nanoparticles due to the large amount of N-based groups on the surface [37–42]. More importantly, the work function of most noble metals is located between the conduction band and the valence band of g-C_3N_4, which will greatly promote the transfer of photogenerated electrons from the g-C_3N_4 to the metal nanoparticles due to Mott-Schottky effects, thereby improving the efficiency of the photocatalytic reaction. Furthermore, Au, Ag and Cu metal

---

nanoparticles can capture the irradiation energy, resulting in high energy electrons on their surface via the localized surface plasmon resonance (LSPR) effects [43–49]. As a result, these high energy electrons on the plasmonic metals would be migrated to the catalytic active sites such as Pd metals. All above inspired us to synthesize Pd-based alloy containing plasmonic metal nanoparticles supported on carbon nitride to design Mott-Schottky catalyst for the photocatalytic hydrogen evolution from formic acid.

Herein, we report the synthesis of a series of well-dispersed AuPd alloy nanoparticles on super small carbon nitride nanospheres (Au_xPd_y/CNS) for the photocatalytic hydrogen evolution from formic acid and aldehyde. These catalysts with different molar ratios of Au/Pd exhibited remarkably enhanced catalytic activity under visible light irradiation than that in the dark. The highest photocatalytic activity with an initial TOF value of $1017.8\,h^{-1}$ was obtained at 298 K. XPS analysis, photoelectrochemical characterization and DFT calculation indicate that the remarkable photocatalytic activities are mainly attributed to the synergistic combination of alloying, plasmonic and Mott-Schottky effects, which can efficiently accelerate the electron transfer from photoresponsive super small carbon nitride nanospheres and plasmonic Au to the active Pd sites. We also found that the alloying effect is the main factor on the high activity, which is mainly attributed to weakened adsorption of hydrogen atoms on Pd sites according to the DFT calculation.

2. Experimental

2.1. Materials

All reagents were analytical grade and used without further purification. Triblock copolymer $EO_{106}PO_{70}EO_{106}$ (Pluronic F127, Mw = 12600) was purchased from Sigma-Aldrich Company Ltd. (U.S.A.). Tetramethoxysilane (98%, TMOS), cyanamide (95%), $HAuCl_4$ and $PdCl_2$ were obtained from Aladdin. Other chemicals were obtained from Shanghai Chemical Reagent.

2.2. Synthesis of AuPd/CNS

Carbon nitride nanospheres (CNS) were synthesized according to the reported method [50]. AuPd/CNS photocatalysts were prepared by impregnating of CNS with $HAuCl_4$ and H_2PdCl_4 aqueous solution, and then reducing with $NaBH_4$. Typically, 0.5 g of CNS was dispersed in 20 mL of deionized water and ultrasonicated for 1 h. Subsequently, a certain amount of $HAuCl_4$ and H_2PdCl_4 (mole ratio = 1:0, 2:1, 1:1, 1:2, 0:1) aqueous solution were added into the CNS suspension under magnetic stirring. After 10 h, 2 mL of $NaBH_4$ aqueous solution (0.1 M) was added dropwise into the mixture under continuous vigorous stirring. After 12 h, the samples were collected by centrifugation and washed with deionized water. Finally, the products were dried at 60 °C overnight. The obtained sample was denoted as Au/CNS, Au_2Pd_1/CNS, AuPd/CNS, Au_1Pd_2/CNS and Pd/CNS, respectively.

2.3. Characterization

Powder X-ray diffraction (XRD) patterns were performed on a Rigaku D/MAX-2500 diffractometer, under a filtered Cu-Kα radiation source (λ = 1.54056 Å) at a scan rate of 3°/min. The Fourier transformed infrared spectra (FTIR) was obtained by a Nicolet Magna 670 FTIR spectrometer using KBr pellets technique. The nitrogen adsorption-desorption isotherms were recorded by using a Micromeritics Trisstar 3000 instrument at 77 K. The specific surface area was determined according to the Brunauer-Emmett-Teller model. Transmission electron microscopys (TEM) were taken with a Philips Tecnai G2 F20 system at an accelerating voltage of 200 kV. The UV–vis diffuse reflectance spectra of photocatalysts were measured on a Varian

Cary 500 Scan UV–vis spectrophotometer with $BaSO_4$ as the reflectance standard. X-ray photoelectron spectroscopy (XPS) was conducted on a PHI 1600 (PerkinElmer). All spectra were recorded at room temperature and the binding energy was referred to C 1 s peak at 284.8 eV. Photoluminescence spectra (PL) were done on Jobin Yvon Fluorolog3-21 spectrophotometer at an excitation wavelength of 380 nm. Electrochemical measurements were carried out with an Autolab 302 N Electrochemical System and used an Ag/AgCl (0.5 M Na_2SO_4) as the reference electrode and a Pt plate as the counter electrode.

2.4. Photocatalytic H_2 evolution from formic acid

The photocatalytic H_2 production experiments were carried out in a closed 400 mL reactor vertically irradiated by a 300 W high-performance simulated sunlight xenon lamp (PLS-SXE300C, Beijing Perfectlight. Co., Ltd.). In a typical experiment, AuPd/CNS (0.04 mmol AuPd) was added to a fresh 1.0 M of HCOOH and HCOONa (mole ratio = 4:1) solution (100 mL) after being purged with N_2 for 0.5 h in a closed 400 mL reactor with circulating cooling water. The reaction was operated at room temperature with a visible light (λ > 420 nm) illumination. The gas molecules generated in the head space were periodically analyzed quantitatively by a Bruker 456 gas chromatograph equipped with a thermal conductivity detector (TCD).

2.5. DFT computational methods

DFT calculations were performed by using the Vienna Ab Initio Simulation Package (VASP). The ion-electron interaction was described using the projector-augmented plane wave (PAW) approach. The Perdew-Burke-Ernzerhof (PBE) functional and plane-wave basis set with a cutoff energy of 400 eV was selected for the calculations. The van der Waals interactions were described using the empirical DFT + D3 method. All structures were relaxed until the maximum force on the movable atoms was less than 0.02 eV/Å. A 2 × 2×1 supercell g-C_3N_4 model is established. The vacuum space was more than 15 Å to avoid the interactions between period images. The surface Brillouin zone was sampled by a 3 × 3 k point mesh.

3. Results and discussion

Super small carbon nitride nanospheres decorated with AuPd alloy nanoparticles were synthesized by a simple liquid phase reduction process (Fig. 1a). First, the cyanamide was impregnated into the inner cages of hollow SiO_2 spheres as our previous method [51], which was transferred into g-C_3N_4/SiO_2 through the thermal polymerization at high temperature. The final carbon nitride nanospheres (CNS) could be obtained by removing the SiO_2 template. Subsequently, using super small carbon nitride nanospheres as the supports, a series of bimetallic AuPd nanoparticles were prepared by the co-reduction method of $HAuCl_4$ and H_2PdCl_4 with $NaBH_4$ as reductant.

The microstructure and the AuPd distribution of the as-prepared photocatalyst were investigated by TEM. As shown in Fig. 1b, the carbon nitride nanosphere shows an uniform structure with a diameter of about 20 nm, which is in good agreement with the SiO_2 hollow nanospheres (Fig. 1c), indicating a good replicate from templates. The TEM images of the as-prepared AuPd alloy show that almost all the nanoparticles are homogeneously distributed on the surface of carbon nitride nanosphere with an average size of 3.0 ± 0.5 nm (Fig. 1d and f). The fine distribution of AuPd nanoparticles on CNS may be due to the stabilization effect of uncondensed amine groups on the surface of carbon nitride [37–42]. A lattice fringe of 0.230 nm between those of the (111) planes of fcc Au (0.236 nm) and fcc Pd (0.227 nm) is observed in the HRTEM of AuPd/CNS (Fig. 1d inserted), indicating the formation of the AuPd alloy. In addition, the formation of AuPd alloy structure was further confirmed by the line-scan EDX analysis (Fig. 1d inserted).
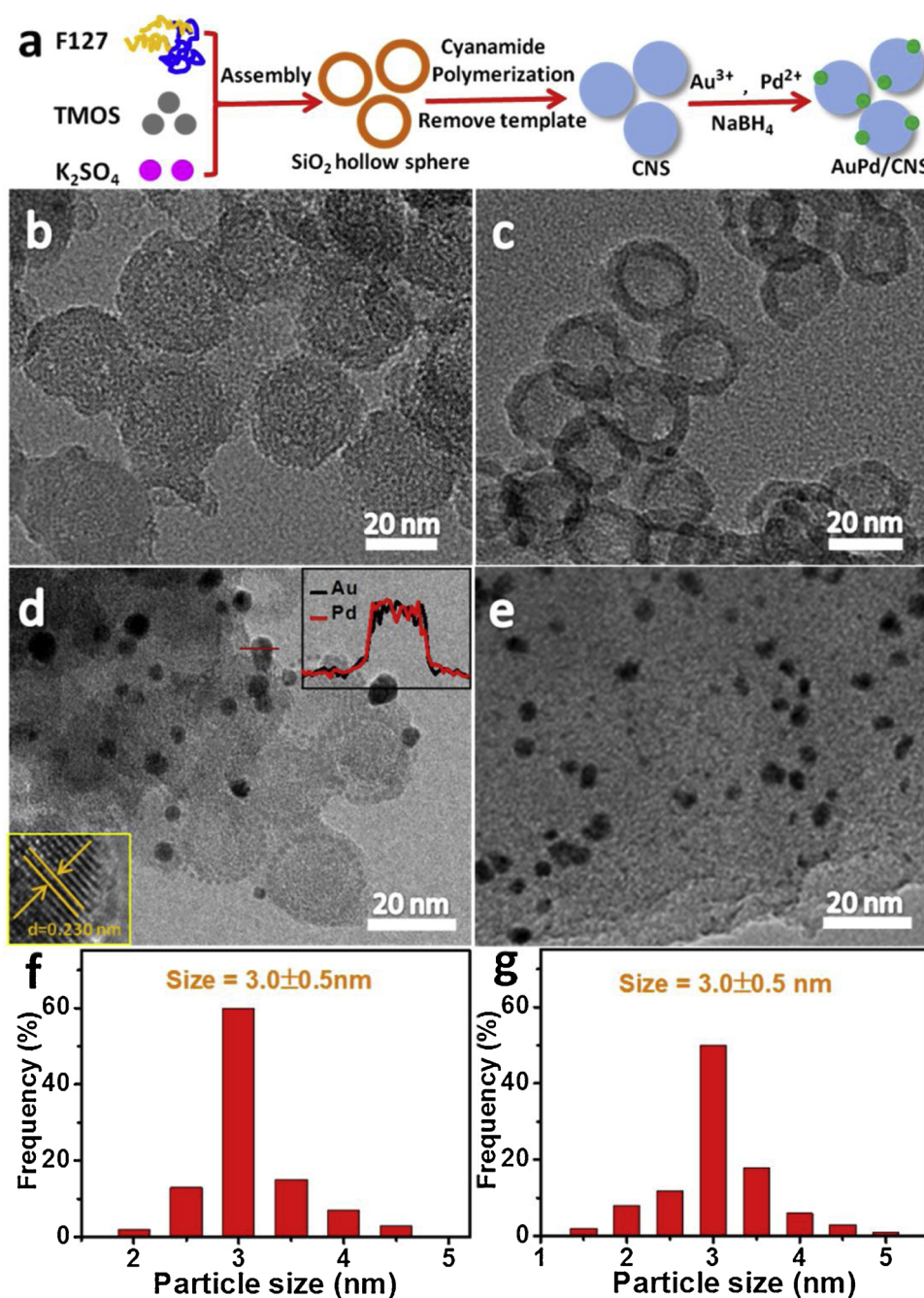
Fig. 1. (a) Synthetic routes of AuPd/CNS. TEM images of (b) carbon nitride nanosphere, (c) hollow SiO_2 spheres, (d) AuPd/CNS (Insets are the HRTEM image and line-scanning analysis for Au and Pd of AuPd/CNS), (e) TEM image of AuPd/Bulk CN, (f) the average diameter histogram of PdAu nanoparticles for AuPd/CNS and (g) the average diameter histogram of PdAu nanoparticles for AuPd/ Bulk CN.

As comparison, AuPd alloy was also supported on the bulk carbon nitride with an average size of 3.0 ± 0.5 nm (Fig. 1e and g), denoted as AuPd/Bulk CN.

The wide-angle X-ray diffraction (XRD) patterns of AuPd alloy supported on carbon nitride with different Au/Pd ratios were shown in Fig. 2a and Figure S3. For Au or Pd monometallic nanoparticles loaded on CNS, the diffraction peaks attributed to Au(111) and Pd(111) could be observed at 2θ = 38.4 and 40.0, respectively. In the patterns of AuPd alloy nanoparticles, the peaks appeared between the two original peaks of Au(111) and Pd(111) and gradually shifted to a higher angle with the increasing of Pd/Au ratio, indicating the formation of the AuPd alloy. The FT-IR spectra of carbon nitride decorated with AuPd nanoparticles were shown in Fig. 2b, the band at 810 cm^{-1} is attributed to the

breathing mode of the triazine ring. Several peaks at 1200-1600 cm^{-1} are associated with the stretching modes of aromatic CN heterocycles. The broad absorption in the range of 3200–3400 cm^{-1} is assigned to N−H stretching mode of amino (e.g., −NH$_2$ or −NH) and O−H stretching vibrations of adsorbed water molecules [31–36,51,52].

X-ray photoelectron spectroscopy (XPS) analysis was carried out to test the electronic states of different elements in AuPd/CNS. In the Pd 3d spectrum (Fig. 3a), the Pd 3d$_{5/2}$ peak of Pd/CNS appear at 335.8 eV. Compared with that of Pd/C (336.0 eV), the binding energy for Pd 3d$_{5/2}$ peak of Pd/CNS is shifted to a lower value, which is mainly due to the electron donation from uncondensed amine groups on the surface of carbon nitride nanospheres. For AuPd/CNS, the binding energy of Pd 3d$_{5/2}$ peak is shifted to a lower value than that of Pd/CNS. At the same
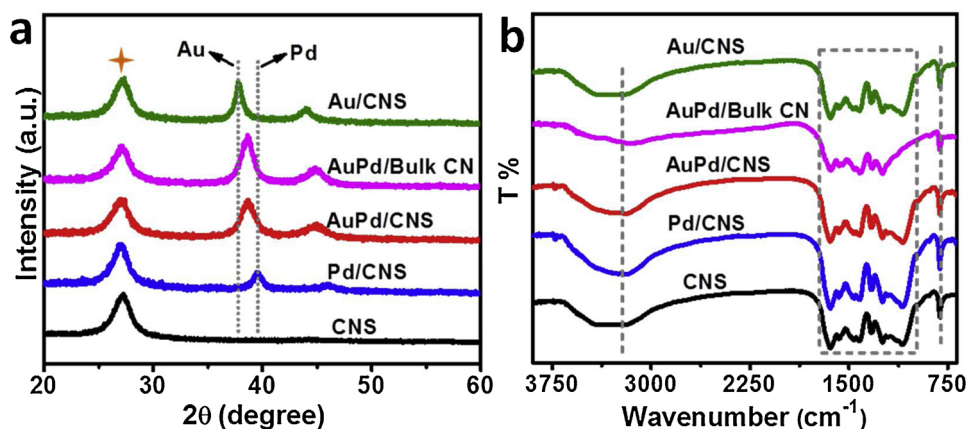
Fig. 2. (a) XRD patterns and (b) FT-IR spectra of CNS, Pd/CNS, AuPd/CNS, AuPd/Bulk CN and Au/CNS.

time, for the Au 4f spectrum (Fig. 3b), the Au $4f_{7/2}$ peak of AuPd/CNS appear at 84.5 eV, corresponding to a higher binding energy than that of Au 4f (84.0 eV) of Au/CNS. These shifts are attributed to the strong interactions and charge redistribution between Au and Pd in the AuPd alloy and some electrons transfer from plasmonic Au to Pd sites. What's more, the binding energy of N 1 s and C 1 s peaks for AuPd/CNS also has an upshift of ˜0.2 eV and ˜0.4 eV, respectively, compared with that of CNS (Fig. 3c,d), because of the electron-donating properties of carbon nitride [26,38,41,53]. These above results indicate that the AuPd alloy and the carbon nitride support are beneficial to increase electron density of Pd.

The optical properties of CNS decorated with Au, Pd and AuPd nanoparticles were studied by the UV/vis diffuse reflectance spectrometry (Fig. 4). It can be observed from Fig. 4 that the background absorption in the visible-light region was enhanced with the doping of metal nanoparticles. In particular, the AuPd/CNS exhibits the strongest visible light absorption, which may be primarily due to the super small nano-size of CNS and alloying effects. Furthermore, the carbon nitride decorated with Au and AuPd nanoparticles exhibited a characteristic absorption peak at 500–550 nm due to the plasmonic effect of Au nanoparticles [13,22,24,47–49].

Subsequently, the catalytic hydrogen evolution from formic acid of all the as-prepared AuPd samples was tested in a 100 mL of 1.0 M HCOOH and HCOONa (mole ratio = 4:1) solution containing 0.04 mmol of AuPd at 298 K. The evolved gas is equal molar amount of H_2 and CO_2 without CO in the reaction system, which was crucial for fuel cell applications. The time profile plots of generated gas (H_2 and CO_2) are shown in Fig. 5a in the dark condition. It can be clearly seen that there was almost no gas formation using the only CNS or Au/CNS. When Pd metal is introduced, gas was immediately generated without
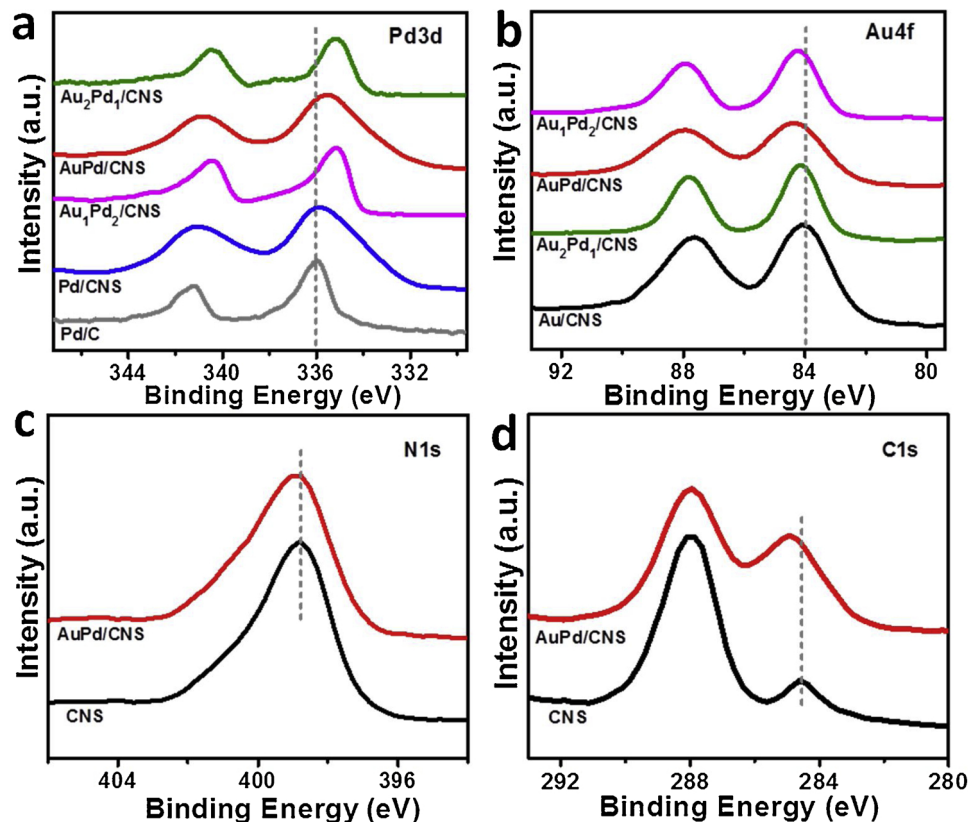

Fig. 3. (a) The XPS of Pd 3d regions of Pd/C, Pd/CNS, Au_1Pd_2/CNS, AuPd/CNS and Au_2Pd_1/CNS. (b) The XPS of Au 4f regions of Au/CNS, Au_2Pd_1/CNS, AuPd/CNS and Au_1Pd_2/CNS. (c) The XPS of N 1 s regions and (d) the xPS of C 1 s regions of AuPd/CNS and CNS.
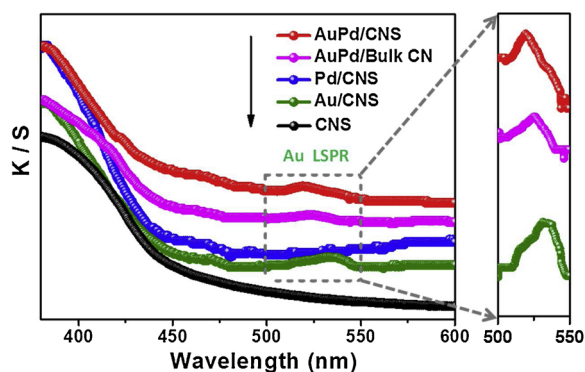
Fig. 4. UV-vis diffuse reflectance absorption the enlarged spectra of CNS, Au/CNS, Pd/CNS, AuPd/CNS and AuPd/Bulk CN.

the induction period and the amount of gas was increased linearly to 86, 137 and 171 mL after 25 min for Pd/CNS, AuPd/Bulk CN and AuPd/CNS, respectively, indicating that the metal Pd is a true catalytic active center. It was also found that the catalytic activity of bimetallic AuPd were higher than that of monometallic Pd under the same conditions. The higher activity of AuPd alloys could be primarily attributed to the strong interactions and charge redistribution between Au and Pd, which accelerates the decomposition of formic acid [13,18,21–26]. Notably, all Pd-containing catalysts performed an enhanced activity under visible light irradiation compared to the dark condition (Fig. 5b). In particular, AuPd/CNS exhibited the highest activity with a high TOF value of 1017.8 h^{-1} under visible light irradiation with λ > 420 nm and the largest activity ratio of 1.52 (activity under light divided by activity under dark) (Fig. 5c, Table 1), which was higher than that of the most reported catalysts at the same temperature (Table S1). About 217 mL gas was generated within 25 min for AuPd/CNS, 46 mL higher than that in the dark, which may be primarily due to the electron donation from the CNS support due to the Mott-Schottky effect and electron redistribution between Au and Pd resulting from alloying and plasmonic effects under visible light-driven condition

Table 1
Physicochemical properties of different materials.

Catalysts	S_{BET}[a] (m^2/g)	Au[b] (wt%)	Pd[b] (wt%)	AuPd Final composition (mol/mol)	TOF (h^{-1})[c]
CNS	112	–	–	–	–
Au/CNS	102	4.52	–	1:0	–
Pd/CNS	104	–	2.54	0:1	418.5
Au$_2$Pd$_1$/CNS	98	3.01	0.81	1.99:1	642.3
AuPd/CNS	101	2.39	1.34	0.96:1	1017.8
Au$_1$Pd$_2$/CNS	97	1.48	1.61	0.49:1	748.9
AuPd/Bulk CN	7	2.42	1.32	0.98:1	745.4

[a] The BET surface areas were calculated using the data in the relative pressure range of P/P$_0$ = 0.05~0.25.
[b] The ICP-AES results.
[c] TOF was calculated from the data within the first 10 min under visible-light according to the following equation: TOF = $n_{gas\ produced}$ / (n_{AuPd} × h).

[13,22,24,54–56]. In order to investigate the Mott-Schottky effect (support effect) on the photocatalytic performance, AuPd alloy was also supported on bulk carbon nitride (noted as AuPd/Bulk CN) with a low specific surface area of ~7 m^2/g. Clearly, the catalytic performance of AuPd/CNS is significantly higher than that of AuPd/Bulk CN, which is mainly due to the large specific surface area of CNS (~100 m^2/g) and the fact that ultra-small CNS can effectively shorten the electron transport path between the support and metal.

To further confirm the contribution of alloying and plasmonic effects under visible light irradiation, a series of AuPd alloys with different Au/Pd molar ratios (Au/CNS, Au$_2$Pd$_1$/CNS, AuPd/CNS, Au$_1$Pd$_2$/CNS and Pd/CNS) were synthesized and applied to the hydrogen evolution from formic acid (Fig. 5d). As mentioned above, metal Pd is the true catalytic active species. With the increasing content of Au, it must be accompanied with the decrease of the active center Pd, since the total metal loading is the same. Unexpectedly, the final catalytic performance of AuPd alloys are still significantly higher than that of the monometallic Pd under the same conditions. These results indicate that
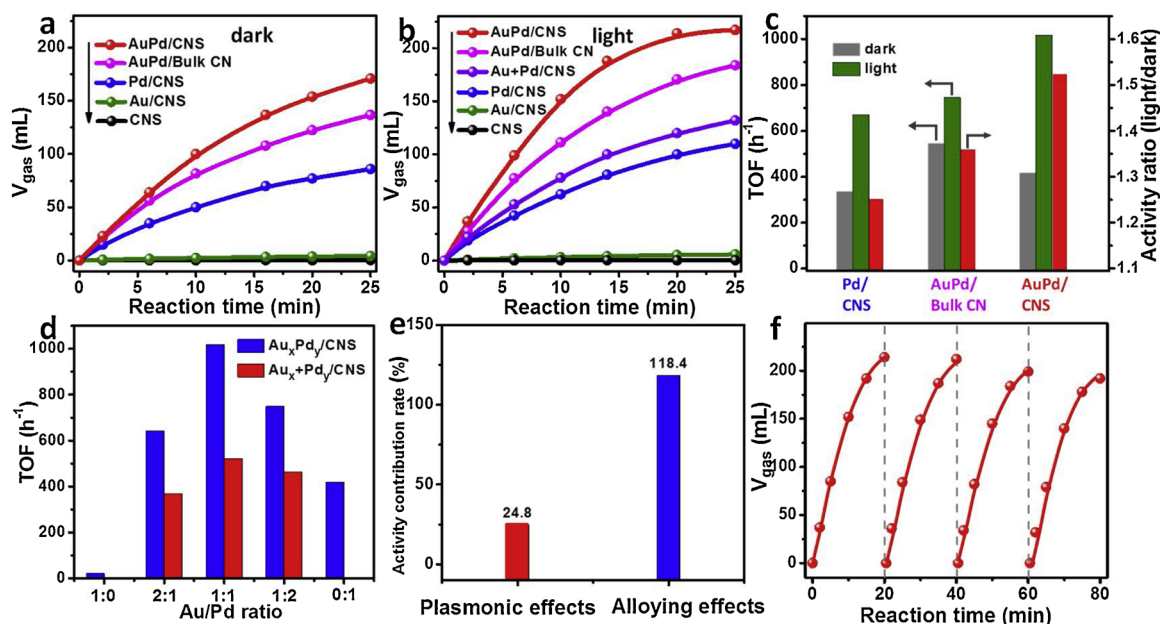

Fig. 5. Time-dependent gas (H$_2$ and CO$_2$) evolution curves from formic acid of all the as-prepared materials (a) in the dark at 298 K and (b) under visible light irradiation (λ > 420 nm) at 298 K. (c) The TOFs and activity ratio of different catalysts in the dark and under visible light irradiation [TOF was calculated from the data within the first 10 min according to the following equation: TOF = mmol$_{gas\ produced}$ /(mmol$_{AuPd}$ × h)]. (d) The TOFs of Au$_x$Pd$_y$/CNS and Au$_x$ + Pd$_y$/CNS under visible light irradiation. (e) The activity contribution rate of alloying effects and plasmonic effects under visible light irradiation. (f) The recycling performance of AuPd/CNS under visible light irradiation (λ > 420 nm).

the alloying and the plasmonic effects caused by visible light-drive have a significant promotion influence on hydrogen production performance. Furthermore, we also tried to approximately estimate the respective contribution from the alloying and plasmonic effects by focusing on the comparison of the reaction activity of the AuPd alloy catalysts (Au_2Pd_1/CNS, AuPd/CNS and Au_1Pd_2/CNS) and physically mixed catalysts ($Au_2 + Pd_1$/CNS, Au + Pd/CNS and $Au_1 + Pd_2$/CNS). As shown in Fig. 5d, the Au + Pd/CNS exhibited the highest activity with a high TOF value of 522.3 h^{-1} among physically mixed catalysts. Compared with Pd/CNS, the activity increasing rate is about 24.8%, which is mainly caused by the plasmonic effect. It happened that AuPd/CNS also exhibited the highest catalytic performance with a high TOF value of 1017.8 h^{-1} in alloy catalysts. Compared with Pd/CNS, the activity increasing rate is about 143.2%. Excluding the plasmonic effect of 24.8% (same as the physically mixed catalyst) [57], the alloying effect accounts for approximately 118.4%, which is ~4.8 times that of plasmonic effects (Fig. 5e). These above results indicate that the performance contribution from the alloying effect is significantly higher than the plasmonic effect, which is consistent with the fact that the formation of the alloy weakens the plasmonic effect according to the literature [13,24,45,55,57].

Furthermore, the reusability experiment was then performed at 20 min intervals to investigate the photocatalytic stability of AuPd/CNS under visible light irradiation (Fig. 5f). After the reaction, AuPd/CNS was recovered by simple filtration and reused for the next run. As shown in Fig. 5f, there was no significant decrease in gas evolution even after the 4th recycle. After the recyclability, the solid catalyst was removed from the reaction system and was characterized by TEM, XRD and FT-IR (Figure S4-6). The TEM image, XRD and FT-IR of AuPd/CNS after the 4th reaction revealed the CNS structures remained and the AuPd nanoparticles were well dispersed without significant aggregation.

In order to exclude the thermal effect arising from light illumination for the enhancement of hydrogen evolution performance, the reaction was carried out without the light irradiation. Obviously, the catalytic activity under visible light irradiation at 298 K was significant higher than that in the dark at 298 K and even higher than that in the dark at 308 K (Fig. 6a). And the temperature variation under visible light irradiation at 298 K is small (about 300 K) by a flow of cooling water. These results suggested that the enhanced activity for AuPd/CNS under visible light irradiation at 298 K was mainly attributed to the light illumination.

It is well known that photocatalytic performance directly depend on the separation and transfer of photogenerated charges for nanocatalysts

[7,13,31–36,50,52]. Therefore, in order to study the photocatalytic mechanism during the reaction, the transfer process of photoinduced charge carriers of AuPd/CNS samples were analyzed by Photoluminescence spectra (PL) under excitation at λ = 380 nm (Fig. 6b). The intensity of PL peak is directly relative to the recombination rate of photoinduced electron-hole pairs. The stronger the PL spectrum intensity, the higher the recombination rate is [31–36,50,52]. Obviously, the Au/CNS, Pd/CNS, AuPd/Bulk CN and AuPd/CNS samples presented the lower peak intensity compared to CNS with the same emission at λ = 460 nm, indicating the highly suppressive recombination of the photogenerated charge carriers due to the formation of heterojunctions between CNS and metal nanoparticles according to the Mott-Schottky effect, which effectively facilitate the interfacial charges transfer and enhance redox capability [27–30]. Especially, AuPd/CNS exhibits the lowest PL intensity, indicating that it has the most efficient charge separation efficiency due to the stronger interaction between the alloy and the super small CNS support. Furthermore, the Mott-Schottky plots of CNS and AuPd/CNS showed that the formation of heterojunctions clearly elevated the conduction band position (Fig. 6c,d), which is helpful to change the electronic environment of embedded metal nanoparticles and their catalytic activities (Fig. 5).

In order to further study the separation efficiency of the photogenerated charges, the transient photocurrent response of carbon nitride supported AuPd alloy nanoparticles were also carried out and shown in Fig. 6e. The photocurrent increased immediately when the light irradiation turned on, while the photocurrent quickly decreased when the light was off, demonstrating the existence of the photoresponse for carbon nitride decorated with AuPd nanoparticles. Moreover, the photocurrent densities of AuPd/CNS and AuPd/Bulk CN catalysts are higher than those of CNS, Au/CNS and Pd/CNS, indicating that the photoinduced electrons and holes on the Au can be rapidly separated and transferred to the Pd surface, which was also evidenced by XPS (Fig. 3). Obviously, AuPd/CNS also shows the higher photocurrent density of about 80 μA/cm² than that of AuPd/Bulk CN (50 μA/cm²), benefiting from the short electron transfer path on the super small carbon nitride nanospheres. In Fig. 6f, the semicircular Nyquist plot of the AuPd/CNS heterojunction sample shows smallest arc radius, indicating AuPd/CNS possesses a better electronic conductivity and more efficient electron separation compared with other samples.

Based on optical performance characterization and catalytic performance comparison, a possible photocatalytic mechanism for hydrogen evolution from formic acid is presented in Scheme 1. In the absence of illumination, formic acid solution undergoes auto-oxidation and reduction reactions only on the active Pd sites of AuPd/CNS by
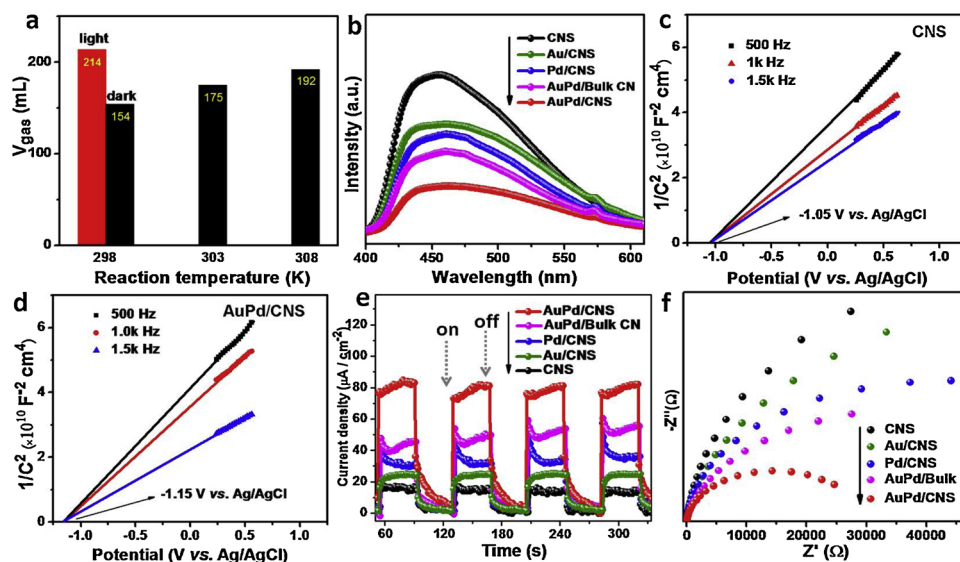

Fig. 6. (a) Effect of temperature under dark and light irradiation (λ > 420 nm) at 20 min for the AuPd/CNS. (b) The photoluminescence spectra of CNS, Au/CNS, Pd/CNS, AuPd/CNS and AuPd/Bulk CN. Mott-Schottky plots of (c) CNS and (d) AuPd/CNS at selected frequencies of 0.5, 1.0 and 1.5 kHz. (e) Transient photocurrent responses and (f) EIS Nyquist plots of CNS, Au/CNS, Pd/CNS, AuPd/CNS and AuPd/Bulk CN.
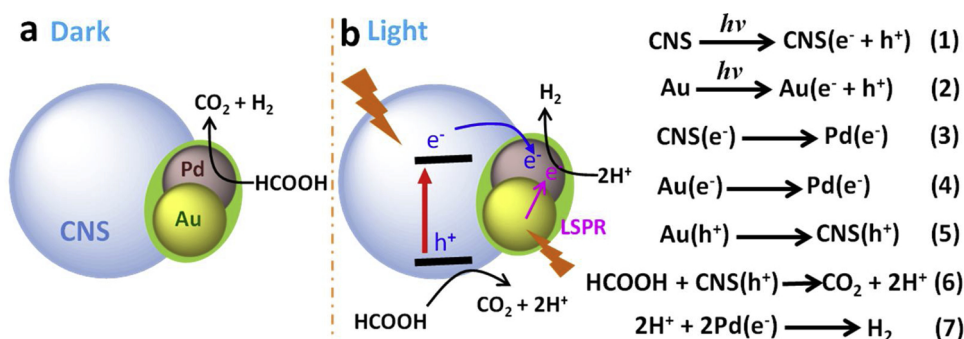
Scheme 1. Schematic illustration of photocatalytic hydrogen evolution from formic acid for AuPd/CNS (a) under dark and (b) light.

thermal catalytic power to produce hydrogen and carbon dioxide. However, when being irradiated with visible light, the electron-electron collisions and electron redistribution between Au and Pd occur due to alloy effects and plasmonic effects, causing electrons to migrate to Pd sites. In addition, the photoresponsive CNS also generates electrons and holes under visible light, and then these generated electrons are transferred to the active Pd sites, resulting in electron-rich active Pd sites. Subsequently, the formic acid is oxidized by holes on the CNS surface to produce CO_2 and protons and then these protons are reduced by electron-rich active Pd sites to release hydrogen. It can be seen that remarkable catalytic activities are mainly attributed to the synergistic combination of alloying, plasmonic and Mott-Schottky effects with assistance of visible-light irradiation, which efficient accelerate the electron transfer from photoresponsive super small carbon nitride nanospheres and plasmonic Au to the active Pd sites.

In addition, DFT theoretical calculations were performed to further explore the interaction between metal and support caused by the Mott-Schottky effect. Herein, we built simple models containing a four-atom metal cluster on g-C_3N_4 for describing Pd/CNS and AuPd/CNS (Fig. 7). On the basis of the Bader charge analysis, in the absence of light, totally 0.37 |e| and 0.44 |e| are transferred from the Pd_4 cluster and Pd_2Au_2 cluster to g-C_3N_4 surface, respectively, indicating a strong electronic interaction between metal clusters and semiconductor (Fig. 7a,b). In particular, there is a stronger interaction between the AuPd alloy and g-

C_3N_4 than that of between the single metal Pd and g-C_3N_4. When the metal-supported g-C_3N_4 catalyst is exposed to continuous illumination, the photoexcited electrons in the conduction band of g-C_3N_4 can be instantly transferred to the surface of PdAu cluster, leaving behind hole localized at the valence band of g-C_3N_4 according to Mott-Schottky effect [27–30]. Electron-rich metals will accelerate the reduction of proton hydrogen, while holes on g-C_3N_4 will accelerate the oxidation of formic acid to release proton hydrogen and CO_2 (Fig. 7c). Furthermore, partial density of states (DOS) of Pd_4 and Pd_2Au_2 clusters on g-C_3N_4 further indicates that the formation of AuPd alloy increases the density of states around the Fermi level (Fig. 7d), which would greatly reduce the Mott-Schottky barrier and accelerate the electron transfer at the support-metal interface.

As mentioned above, the alloying effect play a key role in improving the performance. In order to deeply understand and prove the alloy effects, theoretical calculations at the atomic level are performed. According to the reaction mechanism mentioned above, proton reduction reaction mainly occurs on the electron-rich Pd metal, and thus the adsorption energy of the hydrogen atom on the metal was calculated. As shown in Fig. 7e, adsorption energy values of H atom on Au_2Pd_2/C_3N_4 (-2.41 eV) is significantly less than that of Pd_4/C_3N_4 (-3.95 eV). As known, metal Pd surfaces can easily dissociate hydrogen molecules and intensively bind hydrogen atoms [58]. However, it is difficult for two H atoms to combine to form hydrogen molecules due to strong H atom
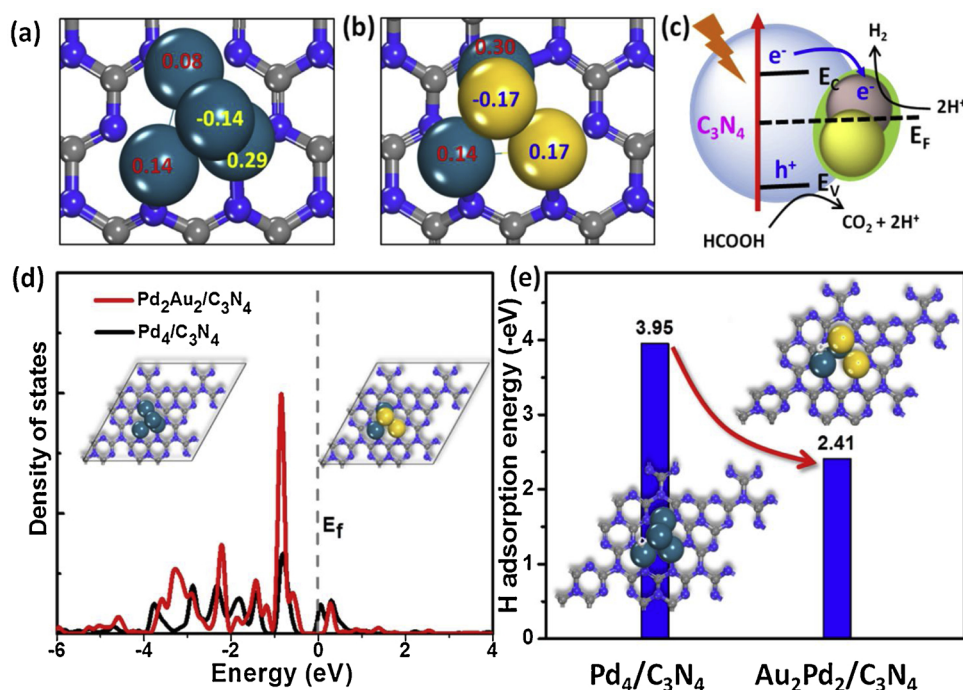
Fig. 7. Bader charges of the (a) Pd_4 and (b) Au_2Pd_2 clusters on the C_3N_4. (c) Schematic view of a Mott-Schottky-type AuPd/C_3N_4 contact (E_F: work function; E_C: conduction band; E_V: valence band). (d) Partial density of states (DOS) of Pd_4 (black line) and Pd_2Au_2 clusters (red line) on C_3N_4. (e) Adsorption energy values of products H atom on Pd_4/C_3N_4 and Au_2Pd_2/C_3N_4. (For interpretation of the references to colour in this figure legend, the reader is referred to the web version of this article).
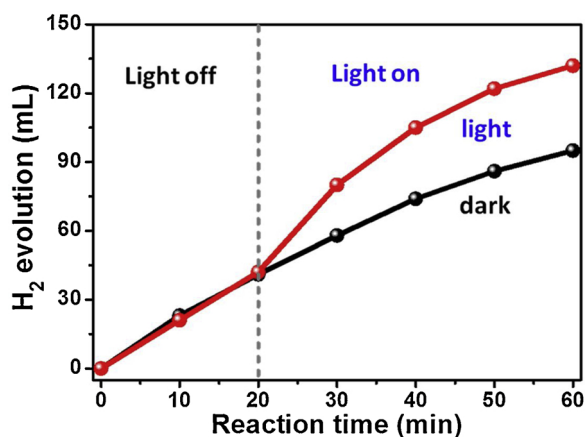
Fig. 8. Time-dependent hydrogen evolution curves from formaldehyde-water solution of the as-prepared AuPd/CNS in the dark at 298 K (black line) and under visible light irradiation ($\lambda > 420$ nm) at 298 K (red line) (For interpretation of the references to colour in this figure legend, the reader is referred to the web version of this article).

Table 2
AuPd/CNS-catalyzed hydrogen evolution from different aldehydes.

Entry	Reagents	Reaction time / h	H_2 / mL dark	light
1	HCHO	1	95	132
2	CH_3CHO	1	31	43
3	CH_3CH_2CHO	1	7	12
4	C_6H_5CHO	1	19	30

Conditions: 0.4 mM AuPd, 1.0 M aldehydes, 1.0 M NaOH, 298 K, $\lambda > 420$ nm.

adsorption for single metal Pd. The simulation results indicate that the addition of inert element Au brings relative weak hydrogen atom adsorption on AuPd alloy, which eventually results in high hydrogen production rate.

Recently, we found that AuPd nanoclusters confined inside amino-functionalized organosilica nanotubes can catalyze visible-light-driven hydrogen evolution from formaldehyde-water solution [13]. In order to explore more applications of AuPd/CNS, we further tried the dehydrogenation of formaldehyde-water solution with a visible light ($\lambda > 420$ nm) illumination at the room temperature. Specifically, the catalytic hydrogen evolution reaction was tested in a 100 mL of 1.0 M formaldehyde-water solution containing 0.04 mmol of AuPd. As shown in Fig. 8, the effect of light irradiation was studied by using AuPd/CNS as a catalyst. In the beginning, the catalytic reaction was monitored within the initial 20 min in dark, and then was continued for the next 40 min under visible-light irradiation. A sudden increase in the reaction rate could be observed from light-off to light-on and the generated hydrogen reached 132 mL within 1 h. In the absence of light, the reaction rate found to be the same as that of activity monitored for initial 20 min and the amount of hydrogen produced was only 95 mL within 1 h. The significant enhancement under light irradiation indicates that light has a significant promotion effect on this reaction.

Besides formaldehyde, other aldehydes, including acetaldehyde, propanal and benzaldehyde are also investigated to produce hydrogen gas. As shown in Table 2, the H_2 amounts from acetaldehyde, propanal and benaldehyde were 31, 7 and 19 mL within 1 h under dark condition, respectively. However, the amount of hydrogen produced was significantly increased to 43, 12 and 30 mL under visible light irradiation, respectively. It is worth mentioning that the electron density of carbon in −CHO for the acetaldehyde and propanal is higher than that of formaldehyde and benzaldehyde. Therefore, it is harder to be attacked by OH^- to form aldehydrol, leading to the decrease in hydrogen evolution amount. These above results indicate the AuPd/CNS catalyst

with synergistic effects has a good universality for photocatalytic hydrogen evolution from liquid-phase chemical hydrogen storage materials.

4. Conclusions

In summary, a series of AuPd alloy nanoparticles on super small carbon nitride nanospheres for the design of Mott-Schottky catalysts were successfully synthesized and further applied for the photocatalytic hydrogen evolution from formic acid. These Mott-Schottky catalysts exhibited remarkably improved catalytic activity under visible light irradiation at 298 K compared with the corresponding thermal catalysts. XPS analysis, photoelectrochemical tests and DFT calculation indicate that the remarkable photocatalytic activities are mainly attributed to the multiple positive factors, including Mott-Schottky, alloying and plasmonic effects, which can efficiently accelerate the electron transfer from photoresponsive super small carbon nitride nanospheres and plasmonic Au to the active Pd sites. Moreover, the AuPd/CNS catalyst presents a good universality for the photocatalytic hydrogen evolution from a series of aldehyde aqueous solutions. This work will provide a guideline on developing and rationally designing Mott-Schottky photocatalysts with synergistic effects for the photocatalytic hydrogen production systems.

Notes

The authors declare no competing financial interest.

Appendix A. Supplementary data

Supplementary material related to this article can be found, in the online version, at doi:https://doi.org/10.1016/j.apcatb.2019.04.013.

References

[1] D. Mellmann, P. Sponholz, H. Junge, M. Beller, Formic acid as a hydrogen storage material-development of homogeneous catalysts for selective hydrogen release, Chem. Soc. Rev. 45 (2016) 3954–3988.

[2] Z. Li, Q. Xu, Metal-nanoparticle-catalyzed hydrogen generation from formic acid, Acc. Chem. Res. 50 (2017) 1449–1458.

[3] J. Willkomm, K.L. Orchard, A. Reynal, E. Pastor, J.R. Durrant, E. Reisner, Dye-sensitised semiconductors modified with molecular catalysts for light-driven H_2 production, Chem. Soc. Rev. 45 (2016) 9–23.

[4] Y.J. Yuan, Z.T. Yu, D.Q. Chen, Z.G. Zou, Metal-complex chromophores for solar hydrogen generation, Chem. Soc. Rev. 46 (2017) 603–631.

[5] M. Wen, K. Mori, Y. Kuwahara, T. An, H. Yamashita, Design and architecture of metal organic frameworks for visible light enhanced hydrogen production, Appl. Catal. B Environ. 218 (2017) 555–569.

[6] Q.L. Zhu, N. Tsumori, Q. Xu, Immobilizing extremely catalytically active palladium nanoparticles to carbon nanospheres: a weakly-capping growth approach, J. Am. Chem. Soc. 137 (2015) 11743–11748.

[7] S. Zhang, M. Li, Q. Wu, H. Yang, J. Han, H. Wang, X. Liu, Photocatalytic hydrogen evolution from formate and aldehyde over molecular iridium complexes stabilized by bipyridine-bridging organosilica nanotubes, Appl. Catal. B Environ. 236 (2018) 466–474.

[8] A. Boddien, D. Mellmann, F. Gärtner, R. Jackstell, H. Junge, P.J. Dyson, G. Laurenczy, R. Ludwig, M. Beller, Efficient dehydrogenation of formic acid using an iron catalyst, Science 333 (2011) 1733–1736.

[9] M. Zacharska, L.G. Bulusheva, A.S. Lisitsyn, S. Beloshapkin, Y. Guo, A.L. Chuvilin, E.V. Shlyakhova, O.Y. Podyacheva, J.J. Leahy, A.V. Okotrub, D.A. Bulushev, Factors influencing the performance of Pd/C catalysts in the green production of hydrogen from formic acid, ChemSusChem 10 (2017) 720–730.

[10] M. Nielsen, E. Alberico, W. Baumann, H.J. Drexler, H. Junge, S. Gladiali, M. Beller, Low-temperature aqueous-phase methanol dehydrogenation to hydrogen and

carbon dioxide, Nature 495 (2013) 85–89.

[11] P. Verma, K. Yuan, Y. Kuwahara, K. Mori, H. Yamashita, Enhancement of plasmonic activity by Pt/Ag bimetallic nanocatalyst supported on mesoporous silica in the hydrogen production from hydrogen storage material, Appl. Catal. B Environ. 223 (2018) 10–15.

[12] H. Hu, Z. Jiao, J. Ye, G. Lu, Y. Bi, Highly efficient hydrogen production from al-kaline aldehyde solutions facilitated by palladium nanotubes, Nano Energy 8 (2014) 103–109.

[13] S. Zhang, H. Wang, L. Tang, M. Li, J. Tian, Y. Cui, J. Han, X. Zhu, X. Liu, Sub 1 nm aggregation-free AuPd nanocatalysts confined inside amino-functionalized orga-nosilica nanotubes for visible-light-driven hydrogen evolution from formaldehyde, Appl. Catal. B Environ. 220 (2018) 303–313.

[14] J. Eppinger, K.-W. Huang, Formic acid as a hydrogen energy carrier, ACS Energy Lett. 2 (2017) 188–195.

[15] M.A. Ziaee, H. Zhong, C. Cui, R. Wang, Additive-free hydrogen generation from formic acid boosted by amine-functionalized imidazolium-based ionic polymers, ACS Sustainable Chem. Eng. 6 (2018) 10421-10128.

[16] F. Wang, J. Xu, X. Shao, X. Su, Y. Huang, T. Zhang, Palladium on nitrogen-doped mesoporous carbon: a bifunctional catalyst for formate-based, carbon-neutral hy-drogen storage, ChemSusChem 9 (2016) 246–251.

[17] S. Zhang, B. Jiang, K. Jiang, W.B. Cai, Surfactant-free synthesis of carbon-supported palladium nanoparticles and size-dependent hydrogen production from formic acid-formate solution, ACS Appl. Mater. Interfaces 9 (2017) 24678–24687.

[18] X. Yang, P. Pachfule, Y. Chen, N. Tsumori, Q. Xu, Highly efficient hydrogen gen-eration from formic acid using a reduced graphene oxide-supported AuPd nano-particle catalyst, Chem. Commun. 52 (2016) 4171–4174.

[19] Q. Wang, N. Tsumori, M. Kitta, Q. Xu, Fast dehydrogenation of formic acid over palladium nanoparticles immobilized in nitrogen-doped hierarchically porous carbon, ACS Catal. 8 (2018) 12041–12045.

[20] Y. Leng, C. Zhang, B. Liu, M. Liu, P. Jiang, S. Dai, Synergistic activation of palla-dium nanoparticles by polyoxometalate-attached melem for boosting formic acid dehydrogenation efficiency, ChemSusChem 11 (2018) 3396–3401.

[21] Y. Ding, W. Sun, W. Yang, Q. Li, Formic acid as the in-situ hydrogen source for catalytic reduction of nitrate in water by PdAg alloy nanoparticles supported on amine-functionalized SiO₂, Appl. Catal. B Environ. 203 (2017) 372–380.

[22] M. Wen, K. Mori, Y. Kuwahara, H. Yamashita, Plasmonic Au@Pd nanoparticles supported on a basic metal-organic framework: synergic boosting of H₂ production from formic acid, ACS Energy Lett. 2 (2017) 1–7.

[23] S. Masuda, K. Mori, Y. Futamura, H. Yamashita, PdAg nanoparticles supported on functionalized mesoporous carbon: promotional effect of surface amine groups in reversible hydrogen delivery/storage mediated by formic acid/CO₂, ACS Catal. 8 (2018) 2277–2285.

[24] P. Liu, X. Gu, H. Zhang, J. Cheng, J. Song, H. Su, Visible-light-driven catalytic ac-tivity enhancement of Pd in AuPd nanoparticles for hydrogen evolution from formic acid at room temperature, Appl. Catal. B Environ. 204 (2017) 497–504.

[25] J.-M. Yan, S.-J. Li, S.-S. Yi, B.-R. Wulan, W.-T. Zheng, Q. Jiang, Anchoring and upgrading ultrafine NiPd on room-temperature-synthesized bifunctional NH₂-N-rGO toward low-cost and highly efficient catalysts for selective formic acid dehy-drogenation, Adv. Mater. 30 (2018) 1703038–1703045.

[26] L. Xiao, Y.-S. Jun, B. Wu, D. Liu, T.T. Chuong, J. Fan, G.D. Stucky, Carbon nitride supported AgPd alloy nanocatalysts for dehydrogenation of formic acid under visible light, J. Mater. Chem. A 5 (2017) 6382–6387.

[27] Y.-Y. Cai, X.-H. Li, Y.-N. Zhang, X. Wei, K.-X. Wang, J.-S. Chen, Highly efficient dehydrogenation of formic acid over a palladium nanoparticle-based Mott-Schottky photocatalyst, Angew. Chem. Int. Ed. 52 (2013) 11822–11825.

[28] Y. Liu, J. Guo, E. Zhu, L. Liao, S-J. Lee, M. Ding, I. Shakir, V. Gambin, Y. Huang, X. Duan, Approaching the Schottky-Mott limit in van der Waals metal-semi-conductor junctions, Nature 557 (2018) 696–700.

[29] S. Cao, H. Li, T. Tong, H.-C. Chen, A. Yu, J. Yu, H.M. Chen, Single-atom engineering of directional charge transfer channels and active sites for photocatalytic hydrogen evolution, Adv. Funct. Mater. 28 (2018) 1802169–1802177.

[30] Y. Li, Z. Wang, T. Xia, H. Ju, K. Zhang, R. Long, Q. Xu, C. Wang, L. Song, J. Zhu, J. Jiang, Y. Xiong, Implementing metal-to-ligand charge transfer in organic semi-conductor for improved visible-near-Infrared photocatalysis, Adv. Mater. 28 (2016) 6959–6965.

[31] X. Wang, K. Maeda, A. Thomas, K. Takanabe, G. Xin, J.-M. Carlsson, K. Domen, M. Antonietti, A metal-free polymeric photocatalyst for hydrogen production from water under visible light, Nat. Mater. 8 (2009) 76–80.

[32] G. Zhang, Z.-A. Lan, X. Wang, Surface engineering of graphitic carbon nitride polymers with cocatalysts for photocatalytic overall water splitting, Chem. Sci. 8 (2017) 5261–5274.

[33] G. Zhang, G. Li, Z.A. Lan, L. Lin, A. Savateev, T. Heil, S. Zafeiratos, X. Wang, M. Antonietti, Optimizing optical absorption, exciton dissociation, and charge transfer of a polymeric carbon nitride with ultrahigh solar hydrogen production activity, Angew. Chem. Int. Ed. 56 (2017) 13445–13449.

[34] G. Zhang, L. Lin, G. Li, Y. Zhang, A. Savateev, S. Zafeiratos, X. Wang, M. Antonietti, Ionothermal synthesis of triazine-heptazine-based copolymers with apparent

quantum yields of 60% at 420 nm for solar hydrogen production from "sea water", Angew. Chem. Int. Ed. 57 (2018) 9372–9376.

[35] J. Lin, Z. Pan, X. Wang, Photochemical reduction of CO₂ by graphitic carbon nitride polymers, ACS Sustainable Chem. Eng. 2 (2014) 353–358.

[36] M. Zhou, P. Yang, R. Yuan, A.M. Asiri, M. Wakeel, X. Wang, Modulating crystal-linity of graphitic carbon nitride for photocatalytic oxidation of alcohols, ChemSusChem 10 (2017) 4451–4456.

[37] Y. Song, J. Qi, J. Tian, S. Gao, F. Cui, Construction of Ag/g-C₃N₄ photocatalysts with visible-light photocatalytic activity for sulfamethoxazole degradation, Chem. Eng. J. 341 (2018) 547–555.

[38] L.-T. Guo, Y.-Y. Cai, J.-M. Ge, Y.-N. Zhang, L.-H. Gong, X.-H. Li, K.-X. Wang, Q.-Z. Ren, J. Su, J.-S. Chen, Multifunctional Au-Co@CN nanocatalyst for highly effi-cient hydrolysis of ammonia borane, ACS Catal. 5 (2015) 388–392.

[39] H. Zhang, X. Gu, P. Liu, J. Song, J. Cheng, H. Su, Highly efficient visible-light-driven catalytic hydrogen evolution from ammonia borane using non-precious metal na-noparticles supported by graphitic carbon nitride, J. Mater. Chem. A 5 (2017) 2288–2296.

[40] W.-D. Oh, L.-W. Lok, A. Veksha, A. Giannis, T.-T. Lim, Enhanced photocatalytic degradation of bisphenol A with Ag-decorated S-doped g-C₃N₄ under solar irra-diation: performance and mechanistic studies, Chem. Eng. J. 333 (2018) 739–749.

[41] T. Ye, D.P. Durkin, N.A. Banek, M.J. Wagner, D. Shuai, Graphitic carbon nitride supported ultrafine Pd and Pd-Cu catalysts: enhanced reactivity, selectivity, and longevity for nitrite and nitrate hydrogenation, ACS Appl. Mater. Interfaces 9 (2017) 27421–27426.

[42] X.-H. Li, X. Wang, M. Antonietti, Mesoporous g-C₃N₄ nanorods as multifunctional supports of ultrafine metal nanoparticles: hydrogen generation from water and reduction of nitrophenol with tandem catalysis in one step, Chem. Sci. 3 (2012) 2170–2174.

[43] P. Verma, Y. Kuwahara, K. Mori, H. Yamashita, Enhancement of Ag-based plas-monic photocatalysis in hydrogen production from ammonia borane by the assis-tance of single-site Ti-oxide moieties within a silica framework, Chem. Eur. J. 23 (2017) 3616–3622.

[44] F. Wang, C. Li, H. Chen, R. Jiang, L.-D. Sun, Q. Li, J. Wang, J.C. Yu, C.-H. Yan, Plasmonic harvesting of light energy for Suzuki coupling reactions, J. Am. Chem. Soc. 135 (2013) 5588–5601.

[45] H. Liu, M. Li, T.D. Dao, Y. Liu, W. Zhou, L. Liu, X. Meng, T. Nagao, J. Ye, Design of PdAu alloy plasmonic nanoparticles for improved catalytic performance in CO₂ reduction with visible light irradiation, Nano Energy 26 (2016) 398–404.

[46] P. Verma, Y. Kuwahara, K. Mori, Yamashita H, Synthesis and characterization of a Pd/Ag bimetallic nanocatalyst on SBA-15 mesoporous silica as a plasmonic catalyst, J. Mater. Chem. A 3 (2015) 18889–18897.

[47] U. Aslam, V.G. Rao, S. Chavez, S. Linic, Catalytic conversion of solar to chemical energy on plasmonic metal nanostructures, Nat. Catal. 1 (2018) 656–665.

[48] U. Aslam, S. Chavez, S. Linic, Controlling energy flow in multimetallic nanos-tructures for plasmonic catalysis, Nat. Nanotech. 12 (2017) 1000–1005.

[49] Z. Zheng, T. Tachikawa, T. Majima, Plasmon-enhanced formic acid dehydrogena-tion using anisotropic Pd-Au nanorods studied at the single-particle level, J. Am. Chem. Soc. 137 (2015) 948–957.

[50] S. Zhang, M. Li, W. Qiu, Y. Wei, G. Zhang, J. Han, H. Wang, X. Liu, Super small polymeric carbon nitride nanospheres with core-shell structure for photocatalysis, ChemistrySelect 2 (2017) 10580–10585.

[51] J. Tang, Jian, P. Liu, H. Wang, Q. Zhong, Yang, Evolution from hollow nanospheres to highly ordered FDU-12 induced by inorganic salts under weak acidic conditions, Micropor. Mesopor. Mater. 127 (2010) 119–125.

[52] M. Li, H. Wang, X. Li, S. Zhang, J. Han, A. Masters, T. Maschmeyer, X. Liu, Organosilica nanotube templates: one-pot synthesis of carbon-modified polymeric carbon nitride nanorods for photocatalysis, ChemCatChem 10 (2018) 581–589.

[53] J.-M. Yan, Z.-L. Wang, L. Gu, S.-J. Li, H.-L. Wang, W.-T. Zheng, Q. Jiang, AuPd-MnOₓ/MOF-Graphene: an efficient catalyst for hydrogen production from formic acid at room temperature, Adv. Energy Mater. 5 (2015) 1500107–1500112.

[54] X. Nie, X. Jiang, H. Wang, W. Luo, M.J. Janik, Y. Chen, X. Guo, C. Song, Mechanistic understanding of alloy effect and water promotion for Pd-Cu bimetallic catalysts in CO₂ hydrogenation to methanol, ACS Catal. 8 (2018) 4873–4892.

[55] Z. Zhang, S.-W. Cao, Y. Liao, C. Xue, Selective photocatalytic decomposition of formic acid over AuPd nanoparticle-decorated TiO₂ nanofibers toward high-yield hydrogen production, Appl. Catal. B Environ. 162 (2015) 204–209.

[56] M. Zhao, H. Xu, S. Ouyang, H. Tong, H. Chen, Y. Li, L. Song, J. Ye, Fabricating a Au@TiO₂ plasmonic system to elucidate alkali-induced enhancement of photo-catalytic H₂ evolution: surface potential shift or methanol oxidation acceleration? ACS Catal. 8 (2018) 4266–4277.

[57] Z. Xu, M. Kibria, B. AlOtaibi, P.N. Duchesne, L.V. Besteiro, Y. Gao, Q. Zhang, Z. Mi, P. Zhang, A.O. Govorov, L. Mai, M. Chaker, D. Ma, Towards enhancing photo-catalytic hydrogen generation: which is more important, alloy synergistic effect or plasmonic effect? Appl. Catal. B: Environ. 221 (2018) 77–85.

[58] W. Dong, J. Hafner, H₂ dissociative adsorption on Pd (111), Phys. Rev. B 56 (1997) 15396–15403.